Integrating detailed power take-off system models in wave energy converter simulations using an FMI-based co-simulation approach

Ocean Engineering 335 (2025) 121651

Contents lists available at ScienceDirect

Ocean Engineering

journal homepage: www.elsevier.com/locate/oceaneng

Research paper

Integrating detailed power take-off system models in wave energy converter simulations using an FMI-based co-simulation approach

Xinyuan Shao [a,*], Jan Forsberg [b], Jonas W. Ringsberg [a]

[a] Chalmers University of Technology, Department of Mechanics and Maritime Sciences, Division of Marine Technology, SE-41296, Gothenburg, Sweden
[b] Karlstad University, Department of Chemical and Engineering Sciences, Division of Environmental and Energy Systems, SE-65188, Karlstad, Sweden

ARTICLE INFO

Keywords:
FMI-based co-simulation
Optimization
Optimal generator parameters
Power take-off system
Wave energy converter

ABSTRACT

The power take-off (PTO) system is a core component of a wave energy converter (WEC) that significantly influences its power performance. Careful design and testing of PTO systems are essential in WEC development. Numerical simulations have largely replaced physical testing, accelerating the PTO system design process. However, one major obstacle still prevents numerical modelling of the PTO system from achieving its full capability: integrating the PTO system model into the global simulation of the WEC system to include the effects of all subsystems. This paper uses a co-simulation approach based on the Functional Mock-Up Interface (FMI) standard to integrate a detailed PTO system model into a global WEC model that includes hydrodynamic, mechanical, and mooring subsystems. The approach is compared against a model incorporating a simplified linear-damper PTO system. The results indicate that a higher-fidelity PTO system model can have a significant impact on predictions of WEC motion, mooring fatigue damage accumulation, and power performance. For example, it is observed that a simplified PTO model can lead to a tenfold underestimation of mooring fatigue damage under some environmental conditions.

1. Introduction

Wave energy is one of the most promising offshore renewable energy sources. Waves store a large quantity of energy, as oceans cover over 70 % of the Earth's surface area, and waves are endlessly generated by friction between wind and surface water. The International Energy Agency (2023) has predicted that the global electricity demand will rise from its current level by over 80 % in the 'stated policies' scenario by 2050 and that the additional demand will be met mainly by low-emission sources. Due to its high energy density and consistency, wave energy can play an important role in the transition to clean energy.

Wave energy converters (WECs) are devices that convert wave energy into electricity. They can be roughly classified into oscillating water column devices, oscillating body systems, and overtopping converters according to their working principles (Falcao, 2010). Although a variety of WEC concepts have been proposed, none have reached commercial maturity. Consequently, the International Energy Agency (2023) predicts that 95 % of the growth in renewable capacity will be in the form of solar and wind power, whose extraction techniques are more mature.

The seemingly dim prospect of wave energy is due to the unique technological challenges in developing WECs. Unlike their solar and wind counterparts, WECs have not converged to a unified shape and working principle, which distracts the focus of scientific research and cost-efficient industrialization. Moreover, WECs consist of multiple deeply coupled subsystems from different fields, such as hydrodynamic, electrical, and mechanical engineering, which need to be designed and tested carefully to ensure that they operate in harmony.

Regardless of its working principles, an oscillating body WEC can be divided into four subsystems: the hydrodynamic, mooring, mechanical, and power take-off (PTO) systems. The modelling of the hydrodynamic and mooring systems can usually be done in a single commercial software, as these are commonly encountered components in many ships and offshore structures. The mechanical system refers to the joints between different components that allow only restricted relative motion. For example, a hydraulic piston rod can only translate along its hydraulic cylinder. The modelling of the mechanical system can be performed using standard rigid dynamics software.

However, the PTO system is challenging to model as it usually contains multiple components that transform mechanical energy into electricity. The accuracy of the model of each component heavily affects the fidelity of the global model and the possibility of achieving advanced optimization of PTO system parameters. For example, the energy conversion that takes place in a hydraulic PTO system involves generators whose efficiency is affected by their revolution speed. Finding the

* Corresponding author.
E-mail address: xinyuan.shao@chalmers.se (X. Shao).

https://doi.org/10.1016/j.oceaneng.2025.121651
Received 28 February 2025; Received in revised form 7 April 2025; Accepted 23 May 2025
Available online 31 May 2025

optimal generator speed is crucial for the performance optimization and design of the PTO system. A linear or Coulomb damping PTO system model is inevitable in the preliminary design phase of a WEC, in which the design of the PTO system has not been finalized. Such models have also proven to be satisfactory in some macroscopic studies, for example, on the interactions between WECs within a wave park (Shao et al., 2023, 2024a,b), but a detailed PTO system model needs to be developed for subtle parameter optimizations. Moreover, as the WEC is a strongly coupled system, the mutual influence between the hydrodynamic system and the performance of the PTO system is not negligible. However, there is a lack of studies in which detailed models of the hydrodynamic and PTO systems are integrated to form a comprehensive global model. Typically, a detailed hydrodynamic model is supplemented by a simplified PTO system model, as in Bao and Yu (2024), Chen et al. (2024), and Quartier et al. (2024), or a detailed PTO system model is coupled with a simplified hydrodynamic system model, as in Zeinali et al. (2024).

Therefore, there are two main challenges in simulating WEC systems. The first is how to build a detailed PTO system model that can be used to determine the optimal generator parameters under different sea states. The second is how to merge the PTO system model with the models of the other subsystems flexibly and effectively to form a global simulation model that can better capture the characteristics of a real WEC system.

The first question is addressed in this paper by developing a detailed hydraulic PTO system model and an optimization algorithm. The detailed PTO system model includes accurate representations of the hydraulic cylinder, accumulator, hydraulic motor, and generator. The optimization process uses the exhaustive method, which tries all possible generator speeds within a range with constant intervals and then targets the generator speed that provides the highest power performance. The second question can be solved by coupling multiple solvers. It is not a new idea to couple different solvers to consider the combined effects of all subsystems. Wang et al. (2024) coupled OpenFAST with WEC-Sim to perform aero-servo-elastic simulations of offshore floating wind turbines. Han et al. (2024) coupled OpenFAST, Ansys Aqwa, and Python scripts to simulate floating hybrid wind–wave energy systems. More examples involving coupling different solvers can be found in Cao et al. (2023), Jin et al. (2023), Lee et al. (2021), Li et al. (2022), Yang et al. (2020), and Zhang et al. (2022). The main difficulty in these approaches is in handling the communication between different solvers. Data synchronization between solvers is a troublesome problem that affects computation speed and efficiency. User-defined dynamic-link libraries (DLLs) are widely used to achieve the necessary data communication; however, this requires substantial programming effort, especially when the number of solvers that need to be coupled is large. Engineers may need to perform extensive research into their communication protocols and interfaces. This may be beyond engineers' expertise and distract them from focusing on pure engineering topics. Moreover, the resulting program may not be portable between different platforms and operating systems, which hinders multidisciplinary collaborations across different teams.

This paper presents a solution for the gap between simple and accurate WEC simulation models by proposing a convenient co-simulation coupling framework based on the Functional Mock-Up Interface (FMI) standard. FMI-based co-simulation has proven its capability in many engineering applications, including cellular energy systems (Venzke et al., 2023), hydraulic excavators (Gan et al., 2023), hydraulic percussion units (Andersson et al., 2021), hybrid vehicles (Yuan et al., 2020), and ships (Hatledal et al., 2020). Like these systems, WECs are composed of multiple subsystems and can be analysed using FMI-based co-simulation. Coupling the detailed PTO system model with other subsystem models under an FMI-based co-simulation framework should enable straightforward and standardized data communication between different solvers (Gomes et al., 2018). The FMI standard is supported by many software packages and tools; a list is maintained by the Modelica Association (2024). A subsystem model developed using FMI-supported software and tools can be exported as a functional mock-up unit (FMU). This is a module with input and output pins that can easily be connected to other FMUs in co-simulation platforms, which provide co-simulation algorithms that orchestrate the global simulation. The FMI-based co-simulation framework frees the engineers from programming and decentralizes the model development process. The models developed by different teams can be integrated easily under a unified platform, which has far-reaching implications for industrial applications.

In the authors' previous work, FMI-based co-simulation has been applied to simplified WECs with the PTO system represented as a linear damper (Shao et al., 2025). In this paper, the PTO system is further modelled in detail, and the generator parameters are optimized to improve the accuracy of power estimates. The object of the case study is WaveEL 3.0, which is an oscillating body WEC designed and developed by Waves4Power AB. It can be further categorized as a point absorber WEC as its horizontal dimension is much smaller than the wavelength. Point absorber WECs are the most prevalent WEC type, and the hydraulic PTO system of WaveEL 3.0 is representative, which is why WaveEL 3.0 was chosen as the research object here for demonstration. In addition to the comprehensive co-simulation model, a linear-damper PTO system model is also built to compare its power performance with that of the detailed PTO system model. Moreover, the influence of the fidelity of the PTO system model on the predicted interaction effects for a wave park is studied by implementing a co-simulation model of a wave park with detailed PTO system models integrated into each WEC.

The structure of the remainder of this paper is as follows: Section 2 introduces the methodology used in the study. Section 3 describes the modelling procedures for each subsystem. Section 4 provides numerical verification by comparing the results of co-simulations with some previous results from simulations using DNV SESAM. Section 5 presents and discusses simulation results, including WEC motion, PTO forces, bumper forces, and WEC power performances. The overall goal is to study an application case of co-simulation in integrating a detailed PTO system model into WEC simulations and demonstrate the necessity of this approach for specific simulation purposes.

2. Methodology

This section introduces the methodology for the WEC subsystem modelling and the integrated global WEC modelling. The approach described here applies to general WECs and is not restricted to certain WEC prototypes.

2.1. Co-simulation model

For a complete WEC system model that includes the hydrodynamic, mooring, and mechanical systems, different commercial software packages need to be coupled to achieve a global simulation. The coupling process involves communication between different solvers. A straightforward way to achieve this is by using FMUs exported by software. All FMUs have standardized interfaces following the FMI standard. Each FMU is an encapsulated black box that takes inputs and gives outputs. They can be easily connected on FMU-supported platforms, such as Simulink, to enable data transfer between different solvers. This frees engineers from heavy programming labour and enables easy integration of different subsystem models from distributed developments.

A diagram of the co-simulation model in this study is shown in Fig. 1. The hydrodynamic and mooring system is set up in Ansys Aqwa (Ansys, 2023a), and the mechanical system is modelled in Ansys Rigid Dynamics (Ansys, 2023b). Both are exported as FMUs. The detailed PTO system model is built in Simulink (Mathworks, 2024). Each subsystem is connected on the Simulink platform to perform a co-simulation.

2.2. Mechanical system

The mechanical system in this paper refers to the overall WEC system that converts input motion and forces into desired motion and forces.

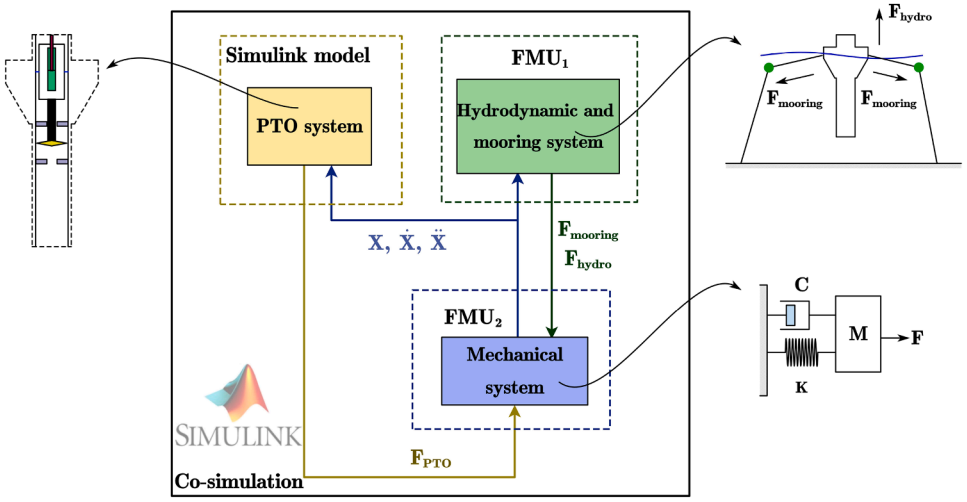

Fig. 1. Diagram of the co-simulation model.

The mechanical system can be fully described by the following equation of motion:

$$\mathbf{M}\ddot{\mathbf{X}} + \mathbf{C}\dot{\mathbf{X}} + \mathbf{K}\mathbf{X} = \mathbf{F}_{\text{hydro}} + \mathbf{F}_{\text{PTO}} + \mathbf{F}_{\text{mooring}} + \mathbf{F}_{\text{other}} \tag{1}$$

where $\mathbf{M}$ is the mass matrix, $\mathbf{X}$ is the position vector, $\mathbf{C}$ is the damping matrix excluding any added damping, $\mathbf{K}$ is the total stiffness matrix, $\mathbf{F}_{\text{hydro}}$ is the sum of the hydrodynamic and hydrostatic loads, $\mathbf{F}_{\text{PTO}}$ is the force from the PTO system, $\mathbf{F}_{\text{mooring}}$ is the force from the mooring system, and $\mathbf{F}_{\text{other}}$ represents all other forces, for example, the wind and current loads, which are not included in the current study. These forces are provided by the models of the subsystems, namely, $\mathbf{F}_{\text{hydro}}$ by the hydrodynamic system model, $\mathbf{F}_{\text{PTO}}$ by the PTO system model, and $\mathbf{F}_{\text{mooring}}$ by the mooring system model.

The WEC system is equivalent to a rigid dynamic system whose motion can be solved by the Ansys Rigid Dynamics module. Moreover, this tool offers variant options of joints and constrictions, which can be used to model the mechanical systems a WEC may have, such as joints between different components.

2.3. Hydrodynamic system

2.3.1. Linear potential theory and boundary element method

The linear potential theory, which is the potential theory modified with some linearizations, is widely used in ocean engineering as it can capture relevant hydrodynamic forces with acceptable complexity. The fundamental equation of the potential theory is the Laplace equation:

$$\nabla^2\phi = 0, \tag{2}$$

where ϕ is the velocity potential. The Laplace equation is derived from the continuity equation under two assumptions: the fluid is incompressible and inviscid, and the flow is irrotational.

The linearizations taken in the linear potential theory are twofold. First, the kinematic and dynamic boundary conditions are linearized by Taylor expansion about the mean free surface, and only the linear terms are kept. Second, the velocity potential is divided into three independent parts: the incident, diffracted, and radiated potentials, which can be solved separately by substituting each into the Laplace equation and applying proper boundary conditions. The boundary element method (BEM) is usually used to solve the Laplace equation to obtain the velocity potentials at different wave frequencies. The Ansys Aqwa BEM solver is used in this study.

The hydrodynamic and hydrostatic loads exerted on the body through pressure can be calculated using the linearized Bernoulli equation:

$$p = -\rho g z - \rho\frac{\partial\phi}{\partial t}, \tag{3}$$

where p is the pressure, ρ is the water density, and z is the vertical position of the body. The sum of the hydrodynamic and hydrostatic loads $\mathbf{F}_{\text{hydro}}$ can be obtained by integrating the fluid pressure p over the wetted surface:

$$\mathbf{F}_{\text{hydro}} = -\iint_{S_w} p\mathbf{n}dS. \tag{4}$$

This can be divided into three terms:

$$\mathbf{F}_{\text{hydro}} = \mathbf{F}_{\text{hydrostatic}} + \mathbf{F}_{\text{excitation}} + \mathbf{F}_{\text{radiation}}. \tag{5}$$

The three terms are the hydrostatic force $\mathbf{F}_{\text{hydrostatic}}$, the excitation force $\mathbf{F}_{\text{excitation}}$, and the radiation force $\mathbf{F}_{\text{radiation}}$. Specifically, $\mathbf{F}_{\text{radiation}}$ can be rewritten as

$$\mathbf{F}_{\text{radiation}} = -\mathbf{A}\ddot{\mathbf{X}} - \mathbf{B}\dot{\mathbf{X}}, \tag{6}$$

where $\mathbf{A}$ and $\mathbf{B}$ are the added mass matrix and added damping matrix, respectively. The added mass and added damping are only relevant to the body geometry, and they can be obtained from BEM solvers.

2.3.2. Time domain analysis

The velocity potentials and related forces described in Section 2.3.1 are calculated in the frequency domain, with the wave frequency denoted by ω. However, when the waves are irregular with components of different frequencies and there are some nonlinear loads such as those from the PTO and mooring system, time domain analyses are necessary. Cummins (1962) derived the following expression for $\mathbf{F}_{\text{radiation}}$ in the time domain:

$$\mathbf{F}_{\text{radiation}} = -\mathbf{A}|_{\omega=\infty}\ddot{\mathbf{X}} - \int_0^t \mathbf{h}(t-\tau)\ddot{\mathbf{X}}(\tau)d\tau, \tag{7}$$

where $\mathbf{A}|_{\omega=\infty}$ is the added mass matrix at infinite frequency and $\mathbf{h}$ is the acceleration impulse response function. Ogilvie (1964) connected the acceleration impulse response function with the added damping in the frequency domain, which is written as

$$\mathbf{h}(t) = \frac{2}{\pi}\int_0^\infty \mathbf{B}(\omega)\frac{\sin(\omega t)}{\omega}d\omega. \tag{8}$$

Therefore, the radiation force in the time domain can be fully described using the hydrodynamic coefficients solved by BEM solvers in the frequency domain.

The other part of the hydrodynamic force, the excitation force, is the summation of the excitation forces caused by the wave components of

different frequencies that form irregular waves. The hydrostatic force can be calculated using a constant hydrostatic matrix computed for the equilibrium position or by integrating the hydrostatic pressure over the transient wetted surface.

2.4. Mooring system and mooring fatigue damage analysis

Mooring systems are indispensable to WECs, as they prevent them from floating away from installation sites and restrict unwanted motions to maximize power generation efficiency. The mooring system usually consists of mooring lines and floaters, which connect different mooring segments. The configuration of the mooring system is designed to fulfil different station-keeping requirements. The modelling process of the mooring system in this study is carried out in Ansys Aqwa, which offers a variety of options for mooring properties.

According to the DNV (2021) standard for fibre ropes, the relative tension, which is the ratio between the real tension and the breaking load, should be used to estimate mooring fatigue damage. This approach is called the relative tension–number of cycles to failure (RN) approach. The mooring fatigue damage is estimated as

$$F = \sum_i \frac{R_i^m}{\alpha} \cdot \gamma_F \tag{9}$$

where i is the index for the i-th tension cycle identified by the rainflow counting (RFC) method (Rychlik, 1987), R_i represents the tension range, m and α are constant parameters with values of 13.46 and 0.259 recommended by the DNV standard, and γ_F is the safety factor, whose value is taken to be 60 according to the DNV standard.

2.5. PTO System

The PTO system is vital in the process of transforming wave energy into electricity. The wave energy is first converted into mechanical energy in the hydrodynamic body of a WEC by driving it to move with the waves. For the point absorber studied in this paper, the PTO system contains a hydraulic cylinder, a hydraulic motor, and a generator. The mechanical energy of the hydrodynamic body is transformed into hydraulic energy in the cylinder to drive the motor. In this process, the linear motion of the WEC is converted into rotations, which can be fed into the generator. The full Simulink model of the PTO system of WaveEL 3.0 is introduced in detail in Section 3.2.

3. Model description

3.1. Hydrodynamic and mooring system model

Fig. 2 shows the real WaveEL prototype in the test site. Fig. 3 presents the configuration of the WaveEL 3.0 WEC system, including the WEC and the moorings. The WEC has an overall length of 18.5 m. The lower section is a hollow cylindrical tube of length 10.7 m, and the middle section is a frustum with a maximum diameter of 8.0 m. Additional details of the WEC's geometry are available in Shao et al. (2023). The WEC is secured horizontally by three mooring legs, enabling vertical movement. Each mooring leg has a submerged floater to connect the two segments of the mooring line, as shown in Fig. 3. The main properties of the hydrodynamic and mooring system are listed in Table 1.

Fig. 2. WaveEL 3.0 full-scale prototype in the test site on the Norwegian coast (Waves4Power, 2024).

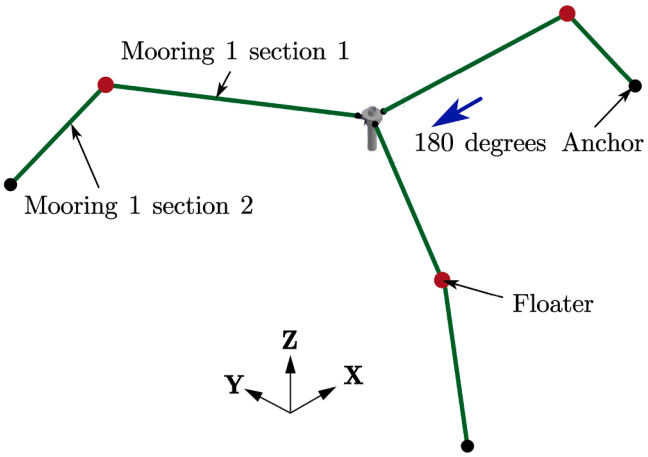

Fig. 3. The mooring configuration of WaveEL 3.0. The blue arrow indicates the wave, which is in the negative x-direction. 180 degrees represents the angle between the wave direction and the positive direction of the x-axis.

3.2. Detailed PTO system model

The detailed PTO system model is a highly complex nonlinear model involving numerous parameters and control methods. The components of the PTO system are illustrated in Fig. 4. For WaveEL 3.0, its PTO system comprises three main interacting components: (1) the buoy hull, (2) the tube water, which is the water inside the acceleration tube, and (3) the water piston. The nomenclature used indicates the forces acting between these components; for example, F_{31} represents the force from component 3 (the water piston) acting on component 1 (the buoy hull). Sections 3.2.1 and 3.2.2 outline the modelling processes for the hydraulic system and the tube water; the full details and equations can be found in Zeinali et al. (2024). The models of the hydraulic motor,

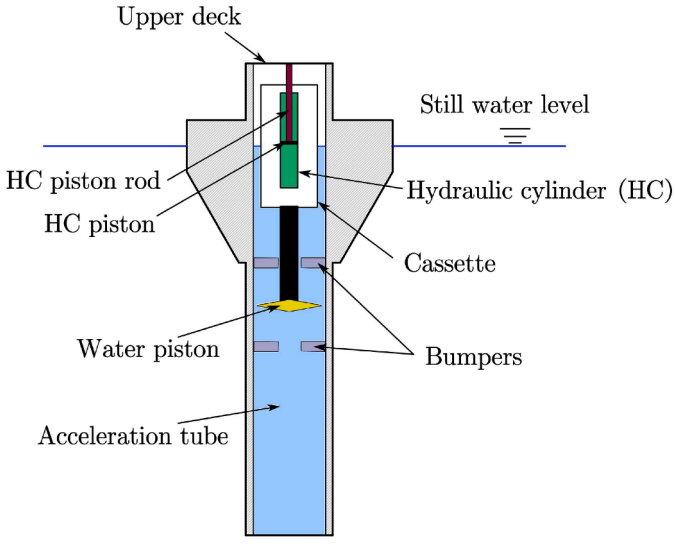

Fig. 4. Inner components of WaveEL 3.0. Note that the accumulation tank and the generator are not shown in this figure.

Table 1
Basic properties of the WaveEL 3.0.

Subsystem	Property	WaveEL 3.0
Hydrodynamic system	Mass [kg]	1.38×10^5
	Draft [m]	15.27
	Volume [m^3]	134.80
	Centre of gravity, COG_w [m][a]	−1.9
	Roll inertia relative to COG_w, I_{xx} [$kg \cdot m^2$]	2.55×10^6
	Pitch inertia relative to COG_w, I_{yy} [$kg \cdot m^2$]	2.55×10^6
	Yaw inertia relative to COG_w, I_{zz} [$kg \cdot m^2$]	1.13×10^6
	Water depth [m]	75
Mooring system	Type	Polyester
	Fairlead depth below still water line [m]	1
	Anchor radius [m]	122.80
	Unstretched mooring line length [m][b]	96; 64.3
	Mooring line diameter [m]	0.08
	Mooring density [kg/m]	4.9
	Mooring unstrained axial stiffness, $EA_{constant}$ [N]	8538
	Mooring axial stiffness coefficient, k_1 [N]	3.00×10^6
	Mooring axial stiffness coefficient, k_2 [N]	3.00×10^7
	Mooring breaking load [kN]	720
	Floater structural mass [kg]	2000
	Floater displaced mass of water [kg]	9430
	Floater added mass [kg]	6700
	Drag coefficient times area [m^2]	7.35

[a] The origin of the reference Cartesian coordinate system is placed in the plane of the water surface at the geometric centre of the WEC buoy when it is in its unloaded neutral position.
[b] The two values are the lengths of the mooring Sections 1 and 2.

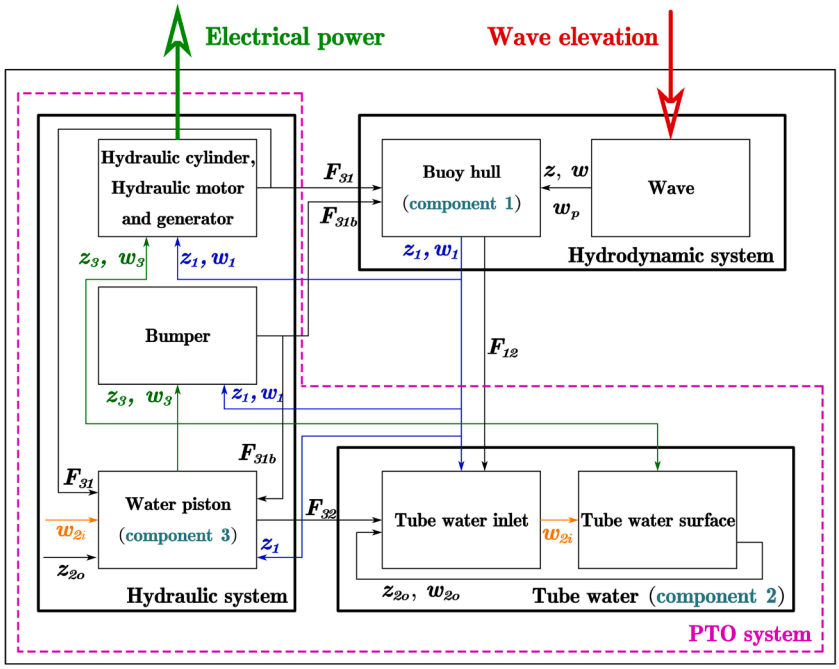

Fig. 5. Diagram of the WEC system's components transforming wave energy into electrical power.

accumulator, and generator are introduced in Section 3.2.3. An overall diagram of the data transfer path between the PTO system model and the simplified hydrodynamic system model is shown in Fig. 5.

3.2.1. *Hydraulic system*

The hydraulic system comprises the hydraulic cylinder, the bumper, and the water piston. The bumper is designed to prevent collisions between the buoy hull and the water piston. The hydraulic circuit and the generator are encapsulated in a watertight cassette, which is connected to the floating water piston. The connection between the cassette–piston assembly and the buoy hull is through the piston rod of the hydraulic cylinder. As the buoy moves with the waves, the relative motion between the buoy and the water piston drives the hydraulic cylinder. These three components are modelled as follows:

- Hydraulic cylinder
  The hydraulic cylinder module uses the position (z_1 and z_3) and velocity (w_1 and w_3) of the buoy hull and water piston, as well as the pressure of the accumulator, as inputs. It outputs the force F_{31} acting on the buoy hull and the pressures at the inlet and outlet of the hydraulic cylinder.

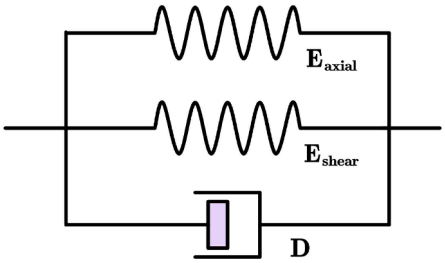

Fig. 6. Bumper Kelvin-Voigt model.

- Bumper
  The bumper module receives the same inputs as the hydraulic cylinder module. Its output is the force F_{31b} acting on the buoy hull. The bumpers are made of rubber to absorb the rapid and intense impacts of the water piston. The reactive force from the bumpers acting on the water piston is simulated using a modified Kelvin–Voigt model. This is illustrated in Fig. 6, in which E_{axial} and E_{shear} represent the stored elastic energy due to axial and shear deformation, respectively, and the dissipated energy is modelled by a damper with a damping coefficient D. Therefore, F_{31b} has three components:

$$F_{31b} = F_{\text{axial}} + F_{\text{shear}} + F_{\text{damping}}. \tag{10}$$

  According to Saccomandi and Ogden (2004), the terms in Eq. (10) can be calculated as follows:

$$F_{\text{axial}} = \frac{\nu kT}{L_0}\left(\lambda - \frac{1}{\lambda^2}\right), \tag{11}$$

$$F_{\text{shear}} = \frac{\nu kT}{3L_0}\left(1 - \frac{1}{\lambda^3}\right), \tag{12}$$

$$F_{\text{damping}} = D\Delta\dot{R}. \tag{13}$$

  Here, λ is the compression ratio of a bumper, which is defined as

$$\lambda = \frac{L_0 - \Delta L}{L_0}, \tag{14}$$

  where L_0 is the free bumper length and ΔL is the compressed length. In addition, $\Delta\dot{R}$ is the rate of change of the bumper's radius. If the bumper is assumed incompressible, then

$$\Delta\dot{R} = \sqrt{\frac{V_0}{4\pi\left(L_0 - \Delta L\right)^3}}\Delta\dot{L}, \tag{15}$$

  where V_0 is the bumper's volume.
- Water piston
  The water piston experiences reactive forces F_{31} from the buoy hull and F_{31b} from the bumper. Its motion is also influenced by the position z_{2o} of the tube water surface and the velocity w_{2i} of the tube water inlet. The primary output of the water piston module is the force F_{32} exerted on the tube water. This force corresponds to the pressure drop resulting from the flow through the narrow gap between the water piston and the acceleration tube wall. For detailed formulae for F_{31}, the reader can refer to the appendix of Zeinali et al. (2024).

3.2.2. Tube water

The dynamics of the tube water are modelled using the conservation laws for mass and momentum. The characteristics of the tube water are represented by the tube water inlet module and the tube water surface module:

- Tube water inlet
  The tube water inlet module takes the force F_{32} from the water piston, the position and velocity of the buoy hull and the tube water surface (z_1, w_1, z_{2o}, and w_{2o}), and the friction force F_{21} (which is equal to F_{12}) from the buoy hull as inputs. The output is the tube water inlet velocity w_{2i}.
- Tube water surface
  The motion of the tube water surface is related to the tube water inlet velocity w_{2i} and the position and velocity of the water piston, z_3 and w_3.

Overall, the outputs of the full PTO system are the two forces F_{31} from the hydraulic cylinder and F_{31b} from the bumper. They are referred to as the PTO force and bumper force in the following sections. The sum of these two forces represents the total force exerted by the PTO system on the buoy hull.

3.2.3. Hydraulic motor, accumulator, and generator

Unlike in Zeinali et al. (2024), the PTO system model presented in this paper includes the conversion process from hydraulic to electrical energy, which is achieved by the hydraulic cylinder, accumulator, hydraulic motor, and generator. Oil from the hydraulic cylinder feeds the accumulator and the hydraulic motor, which converts the translational motion into rotation and drives the generator. The accumulator is filled with nitrogen gas, whose volume changes depending on the relation between the inflow from the hydraulic cylinder and the outflow to the hydraulic motor. The control goal chosen for the generator and the hydraulic motor is to keep their rotation speed constant, which results in a constant oil flow rate and an almost constant generator voltage. A dual-generator setup is used, with ratings of 50 kW and 100 kW. They can work in separate mode (50 kW or 100 kW) or combined mode (150 kW).

The models consider limitations and nonlinearities resulting from the real design and safety requirements. The maximum gas volume of the accumulator is 300 litres. The accumulator is preloaded with a minimum pressure of 2 MPa. The gas pressure is limited to a maximum of 25 MPa by a relief valve. The speed range of the generator is 500–3600 rpm. A throttle valve adjusts the flow rate through the hydraulic motor to prevent it from exceeding 3600 rpm. For safety reasons, the maximum generator speed is limited to 3000 rpm in this study. Moreover, the generator may shift from generator mode to motor mode during short periods when the flow through the hydraulic motor is greater than the instantaneous flow delivered by the hydraulic cylinder and accumulator. Oil from the suction tank is then pumped through a flywheel valve to support the flow of the hydraulic motor. The motor mode is also activated when the generator runs below 500 rpm due to restrictions of the power electronics.

It is assumed that the gas temperature of the accumulator is constant. According to the Boyle's law,

$$p_a V_a = p_0 V_0 \tag{16}$$

where p_a and V_a are the gas pressure and volume at a given moment, and p_0 and V_0 are the gas pressure and volume at the initial state, which in this paper is chosen as 2.3 MPa and 300 litres. The dynamics of the gas pressure are approximated as

$$\frac{dp_a}{dt} \approx -\kappa\frac{p_a^2}{p_0 V_0}\frac{dV_a}{dt} \tag{17}$$

where κ is a coefficient ranging from 1 to 1.4, with 1 for an isothermal process and 1.4 for an isentropic process. To model a real process that is neither isothermal nor isentropic, κ is chosen as 1.2. The gas volume change can be written as

$$\frac{dV_a}{dt} = \frac{dV_m}{dt} - \frac{dV_c}{dt} = \frac{V_{md}}{60}n - A\left(w_3 - w_1\right) \tag{18}$$

where V_c is the oil inflow volume of the hydraulic cylinder, V_m is the oil outflow volume of the hydraulic motor, V_{md} is the displaced oil column of the hydraulic motor, and n is the speed of the hydraulic motor in revolutions per minute. The hydraulic power is calculated as

$$P_h = p_a\frac{dV_c}{dt}. \tag{19}$$

The braking torque M_e of the electric generator is used to control the speed n of the hydraulic motor and thereby the flow through the hydraulic motor. The dynamics of the hydraulic motor can be expressed as

$$\frac{2\pi}{60} J \frac{dn}{dt} = M_m - M_e = \frac{V_{md}}{2\pi} p - M_e \tag{20}$$

where J is the moment of inertia of the joint hydraulic motor and electric generator, and M_m and M_e represent the torque of the hydraulic motor and the electric generator, respectively.

A standard proportional–integral (PI) controller is used to keep the hydraulic motor and electric generator at a set speed. The control error $e = n_{\text{set}} - n$ is input to the PI controller. The required electric torque M_e is determined by

$$M_e = P\left(e + \frac{1}{I}\int_0^t e \, \mathrm{d}\tau\right), \tag{21}$$

where the gain P and integration time I are estimated by standard methods. The electrical power of the generator is calculated as

$$P_e = -M_e \frac{2\pi n}{60}. \tag{22}$$

3.3. Linear-damper PTO system model

A simpler approach to describing the PTO system is to model it as a linear damper with a damping coefficient B_{PTO}, which is 40 kN/m in this study. The time-averaged hydraulic power is calculated as

$$P_{\text{LD}} = \frac{1}{T}\int_0^t B_{\text{PTO}} \dot{z}_1^{\,2} \, dt. \tag{23}$$

3.4. Generator configuration and speed choosing strategy

The generator configuration and speed are crucial variables that determine the electric power performance. Several dimensions need to be considered in the decision process. For safety reasons, the maximum accumulator pressure should not exceed 25 MPa, and the generator speed is restricted to a range from 500 to 3000 rpm. The generator speed is expected to keep a constant value during the operation.

To determine an appropriate generator configuration for a simulated sea state, the wave steepness ($S = 2\pi H_s / gT_p^2$ for irregular waves or $S = 2\pi H / gT^2$ for regular waves) is chosen as a criterion. That is,

$$\begin{aligned} &50\text{kW}: \quad 0 < S \leqslant 0.01, \\ &100\text{kW}: \quad 0.01 < S \leqslant 0.02, \\ &150\text{kW}: \quad S > 0.02. \end{aligned} \tag{24}$$

The optimal generator speed is chosen by following the procedure shown in Fig. 7. The optimization process uses the exhaustive method, which tries all possible generator speeds within a range with constant intervals. Some generator speeds are excluded because they cannot fulfil the requirements of accumulator pressure or cannot be maintained during the operation. Finally, the generator speed that yields the best power performance is chosen.

3.5. Environmental conditions

The analysed environmental conditions (ECs) are listed in Table 2 where H_s is the significant wave height and T_p is the peak period. There are three regular and three irregular wave conditions. The irregular waves follow the JONSWAP wave spectrum with peak enhancement factor $\gamma = 2.4$.

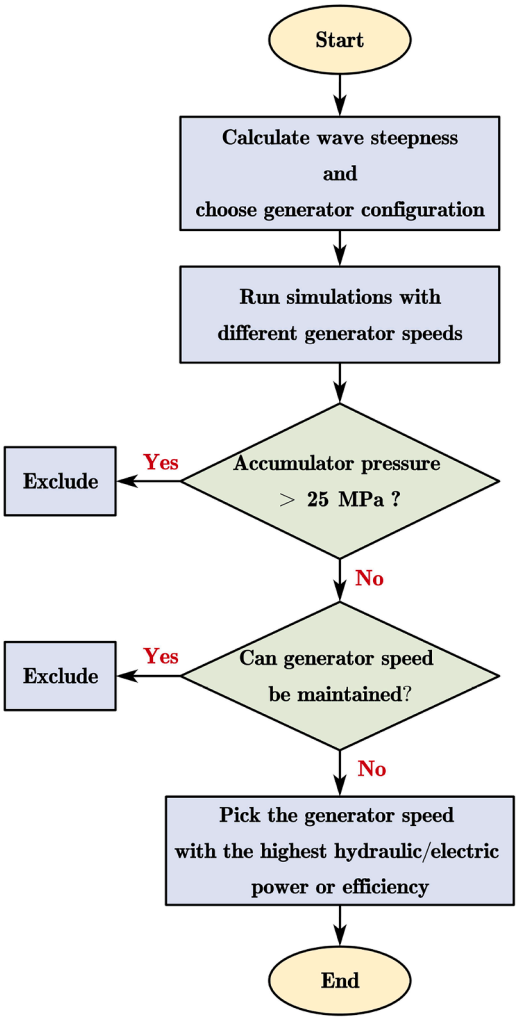

Fig. 7. Generator configuration and generator speed choice strategy.

Table 2
Simulated environment conditions.

	Amplitude A [m]	Period T [s]
EC1	0.25	4.5
EC2	0.75	5.5
EC3	1.75	7.5
	Significant wave height H_s [m]	Peak period T_p [s]
IR-EC1[a]	0.5	4.5
IR-EC2	1.5	5.5
IR-EC3	3.5	7.5

[a] IR stands for irregular wave.

3.6. Wave park configuration

In addition to single-WEC simulations, this study also considers a six-WEC wave park with a hexagonal layout, as shown in Fig. 8. The distance between each WEC is 80 m. The total footprint of the wave park, which is denoted as R, is 139 m. Detailed dimensions can be found in Shao et al. (2024b).

3.7. Coupling the PTO system with the detailed hydrodynamic system

The PTO system and the FMUs of the hydrodynamic, mooring, and mechanical systems are coupled in the Simulink platform, as shown in

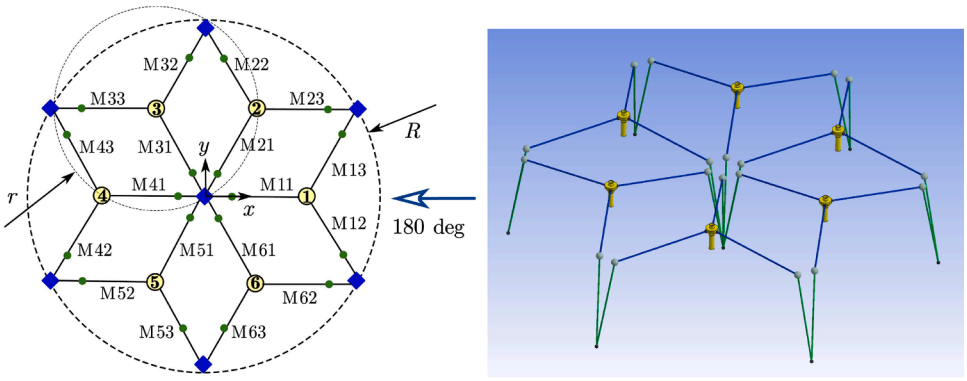

(a) Wave park layout. (b) 3D view.

Fig. 8. Six-WEC hexagonal wave park layout.

Fig. 9(a). The yellow blocks are memory elements to avoid algebra loops. The forces from the PTO system, F_{31}, F_{31b}, and F_{21}, are added to the global force in the vertical direction. For the six-WEC wave park, as shown in Fig. 9(b), each WEC is connected with a detailed PTO system model to form a global simulation.

4. Numerical verification

In this section, the co-simulation method is verified by comparing its power performance predictions for a single WEC and a six-WEC wave park with the results from previous work using DNV SESAM. There are no experimental results for the power performance of this WEC. Therefore, numerical verification is used to support the reliability of the co-simulation approach. In the future, if a single WEC or a wave park is installed in a real physical condition, the co-simulation can be further calibrated and evaluated.

4.1. Single WEC performance

The simulated performances of a single WEC using a linear-damper PTO system model are shown in Fig. 10 for two different modelling frameworks. The simulation model from Shao et al. (2024b) was built in DNV SESAM, whereas the co-simulation model was built following the architecture shown in Fig. 1. The error percentages are less than 8 % for EC3, which is the EC with the largest wave height. This indicates that the two modelling approaches yield similar results for a single WEC using a linear-damper PTO model under regular ECs. The discrepancy may be caused by the slight differences in the mooring system and water depth settings.

4.2. Array park performance

The power performance predictions for a six-WEC array are compared in Fig. 11. Like the single-WEC case compared in Section 4.1, the six-WEC wave park model represents the PTO system as a linear damper. It is observed that the results from co-simulations for these cases show similar interaction patterns to those from DNV SESAM. This comparison verifies the ability of the co-simulation approach to capture the interaction effects between different WECs in a wave park.

5. Results and discussion

5.1. The influence of generator speed

Fig. 12 shows the influence of the generator speed on the mean power performance of a single WEC under three regular ECs. The generator speed range highlighted in red represents the generator speeds that cannot be maintained due to low accumulator pressure. Those highlighted in grey will lead to the generator shifting to motor mode, which will consume instead of producing power. The hydraulic-to-electrical conversion efficiency is defined as the ratio of the mean electrical power to the mean hydraulic power. According to the generator speed-choosing strategy shown in Fig. 7, the generator speeds that lead to a relatively high mean hydraulic power are selected for each EC and applied to further simulations. For EC3, a relatively low generator speed is chosen because increasing the speed results in a slight increase in mean hydraulic power but a significant decrease in mean electrical power and efficiency.

5.2. PTO System and bumper forces

Fig. 13 shows an excerpt of the time history of the PTO force F_{31}, the bumper force F_{31b}, and the motion and velocity responses of the buoy hull (z_1 and w_1) and the water piston (z_3 and w_3). One feature of the detailed PTO system model can be observed in the PTO force curves: the PTO force F_{31} does not vary linearly with the relative velocity as in a linear-damper model. Instead, the mechanism inside the hydraulic cylinder introduces nonlinearity into the PTO forces. There are plateaus in the PTO force curves due to the dynamic valve opening conditions of the suction, outlet, and internal piston valves. For further details of the hydraulic piston model, readers can refer to Section C.1.4 in Zeinali et al. (2024).

The bumper was designed to absorb intense impacts from the water piston and provide reactive force to prevent large displacements. As shown in Fig. 13, the bumper functions only under EC3. When the relative motion ($z_3 - z_1$) between the water piston and the buoy hull is beyond the limited stroke length, which is 1.75 m, the bumper exerts a reactive force on the water piston that is opposite to its motion direction. The peak bumper force can be three times larger than PTO forces, which indicates that it can greatly influence the motion of the WEC.

5.3. WEC Motion

Fig. 14 compares the range of motion of the WECs in the horizontal plane for PTO models with different fidelity levels under three regular ECs. The maritime term ‘watch circle’ is adopted here, which is defined as the circular area in which WECs can move. It is observed that the inclusion of a detailed PTO system model with a higher fidelity results in changes in the size of watch circles and that the size of this effect depends on the wave period and height. It is shown in Fig. 14 that under EC1, WEC 1, which is the first WEC that encounters the incoming wave, is the most sensitive to the changed PTO model. The watch circles of the other WECs, WECs 2 to 6, also tend to expand

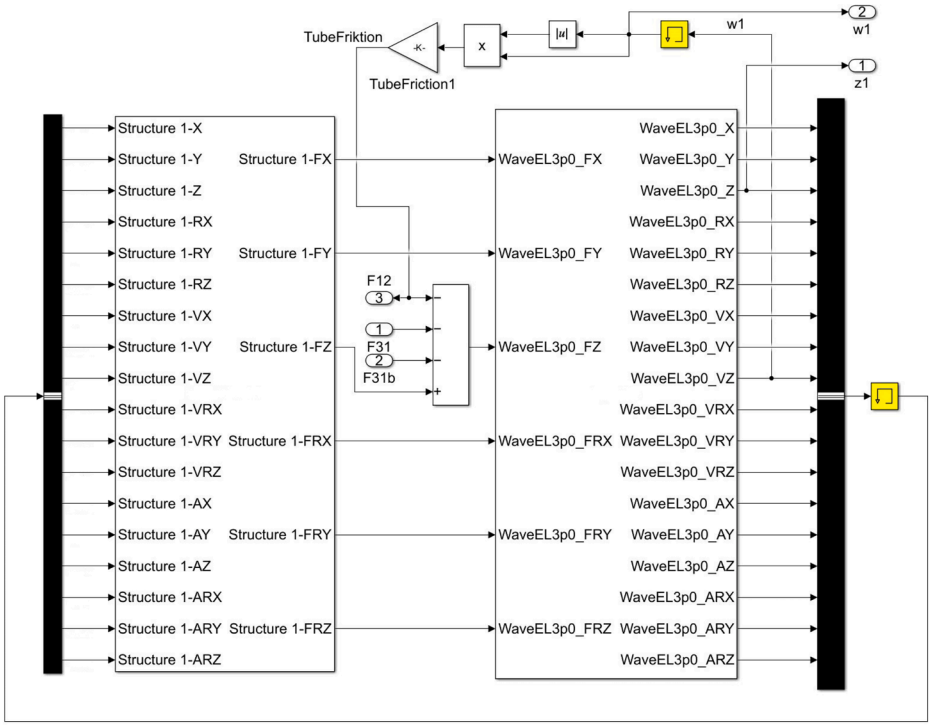

(a) System couplings between the hydrodynamic, mechanical, and PTO models within a single WEC.

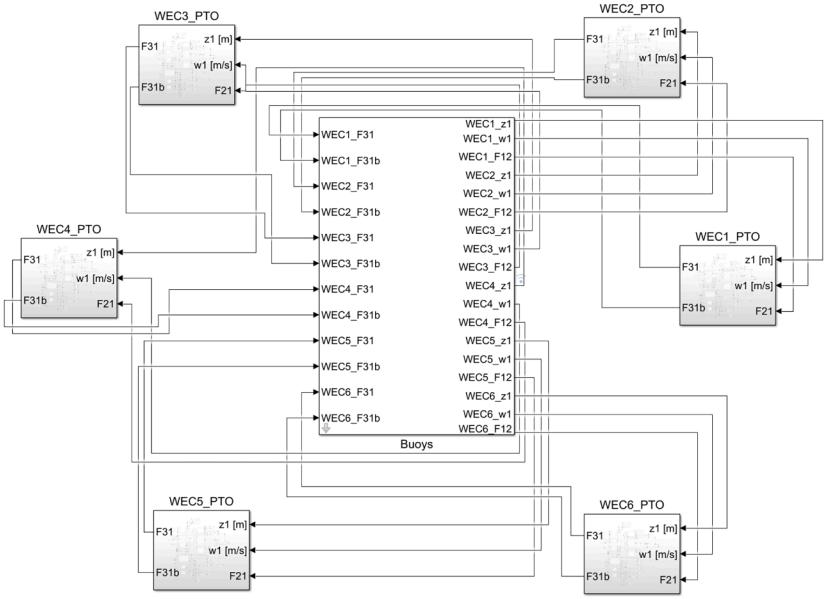

(b) Simulink model for a six-WEC wave park with detailed PTO systems in each WEC.

Fig. 9. Co-simulation model embedded with a Simulink PTO model.

when applying a detailed PTO system under EC1. However, under EC2 and EC3, the range of motion is not strongly affected for any of the WECs by the changed fidelity level of the PTO system model. A possible explanation for this phenomenon is that under mild ECs, when the hydrodynamic forces are relatively small, the inclusion of a nonlinear PTO force will greatly affect the overall dynamic response of the WEC motion, whereas in ECs with larger wave heights, the influence of the nonlinear PTO force on WEC motion responses is minor. The size of the watch circle is crucial in determining the minimum WEC separation distance needed to avoid collisions between WECs and floaters, reduce

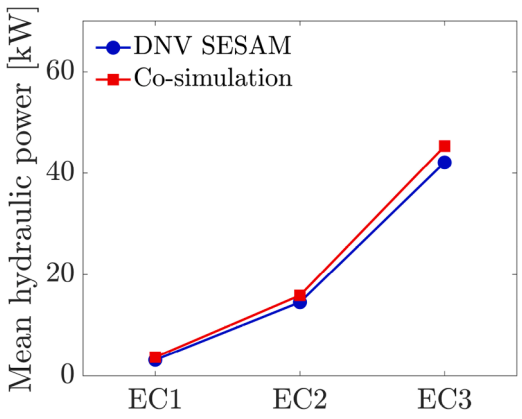

Fig. 10. Single-WEC performance comparison with a linear-damper PTO system model. The results of DNV SESAM come from Shao et al. (2024b).

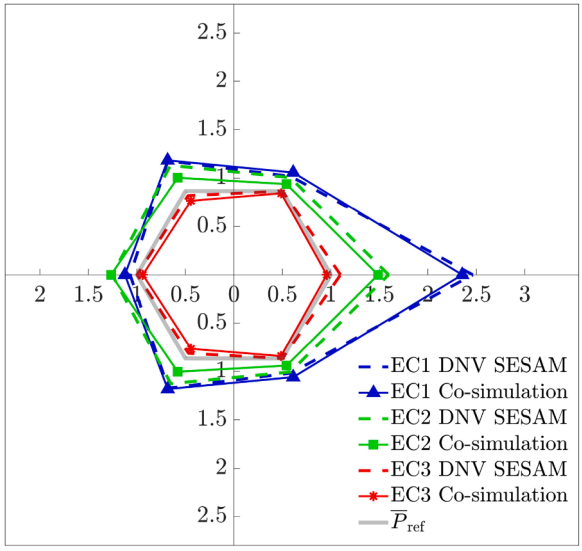

Fig. 11. Wave park performance comparison with a linear-damper PTO system model. The results of DNV SESAM come from Shao et al. (2024b).

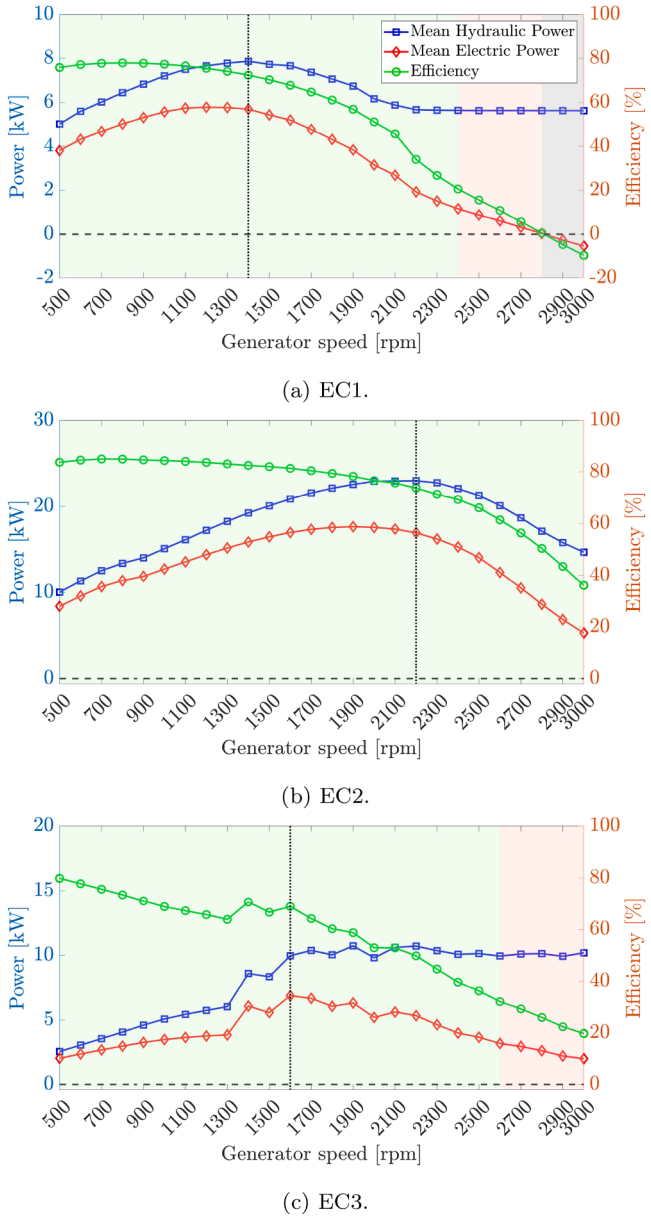

Fig. 12. WEC power performance variation with generator speed. The vertical dotted lines indicate the generator speeds selected for further simulations.

the risk of mooring line entanglement and optimize the mooring and anchoring system design. Therefore, when designing wave parks, the simulation model should include a detailed PTO model to avoid underestimation of the size of the watch circle, especially for compact wave parks.

5.4. Mooring fatigue damage

The mooring lines are subjected to cyclic loads, which lead to fatigue damage over time. As shown in Fig. 14, different PTO models result in different WEC motion range predictions. Therefore, the tension and cyclic stress ranges within the mooring lines, whose main function is to restrict horizontal WEC motion, are also affected when adopting PTO models with different fidelity levels. The global simulations are run for 3600 s to obtain the mooring stress history. The mooring fatigue damage is calculated using Eq. (9) and multiplied by a coefficient of 24×365 to extrapolate the accumulated fatigue damage after one year of operation.

The accumulated mooring fatigue damage at the fairlead of each WEC with a detailed PTO system model under three irregular waves is shown in Fig. 15. The curves indicate the greatest fatigue damage observed for each WEC unit. By comparing these results with Fig. 8, it can be observed that the mooring lines that are aligned with the incoming wave directions are the ones that experience the most fatigue damage in each WEC unit. The magnitude of fatigue damage depends on the severity of wave conditions: from IR-EC1 to IR-EC3, the fatigue damage increases.

Fig. 16 compares the maximum accumulated mooring fatigue damage for each WEC unit observed in the results of global models using a linear-damper PTO model and a detailed PTO system model. The percentages represent the relative increase in the mooring fatigue damage if the PTO system model is upgraded from a linear damper to a detailed PTO system model. In general, the fidelity level of the PTO system model influences the prediction of mooring fatigue damage. The largest discrepancy observed in Fig. 16 occurs in M33 under IR-EC3, for which the fatigue damage is about ten times higher if a detailed PTO system model is used. This is intuitive; because the global model is strongly coupled with all the subsystem models, the fi-

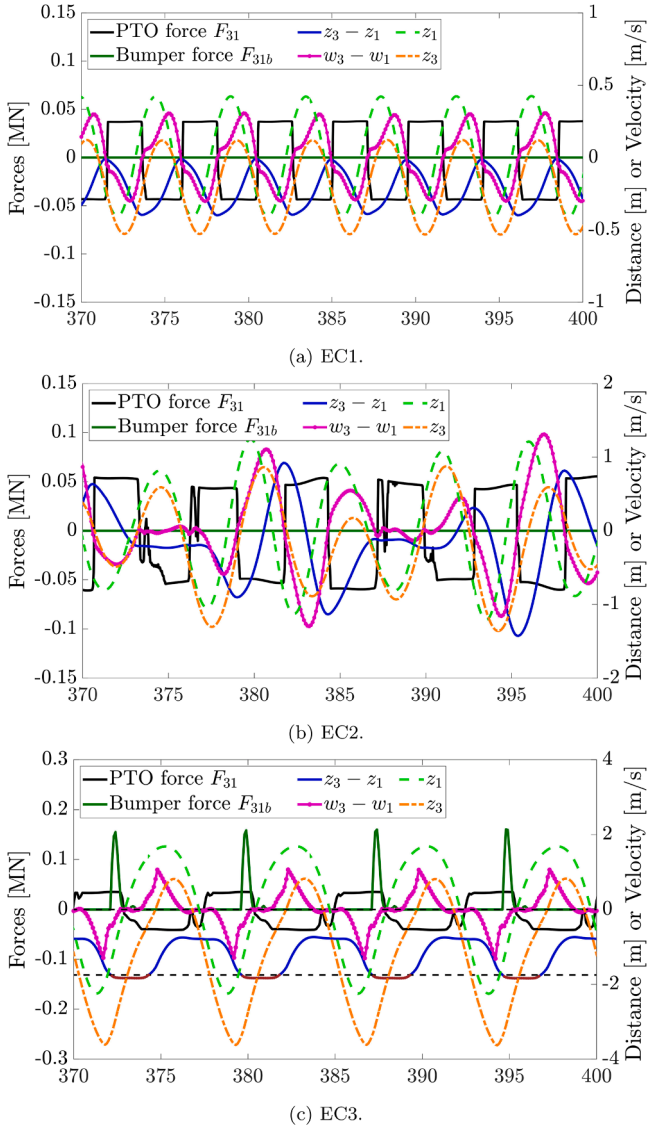

Fig. 13. Forces and motion.

delity level of a subsystem model is expected to affect the results of other subsystem models.

5.5. Influence of the detailed PTO system on wave park performance predictions

5.5.1. Single WEC

The power performance estimates for a single WEC obtained using different PTO system models are compared in Fig. 17. Under EC1 and EC2, the detailed PTO system tends to overpredict the power performance. The discrepancy stems from the difference in how power performance is calculated. The linear-damper model simplifies the whole PTO system to a damping coefficient and calculates the hydraulic power using Eq. (23). The detailed PTO system model considers the inner components of the PTO system and calculates the hydraulic power using Eq. (19). Although the generator speed in the detailed PTO system model and the damping coefficient in the linear-damper PTO model are chosen following the same criterion, which is to attain the 'optimal' power performance, there may still be a mismatch between the generator speed and the damping coefficient. This mismatch leads to the difference between the power predictions under EC1 and EC2.

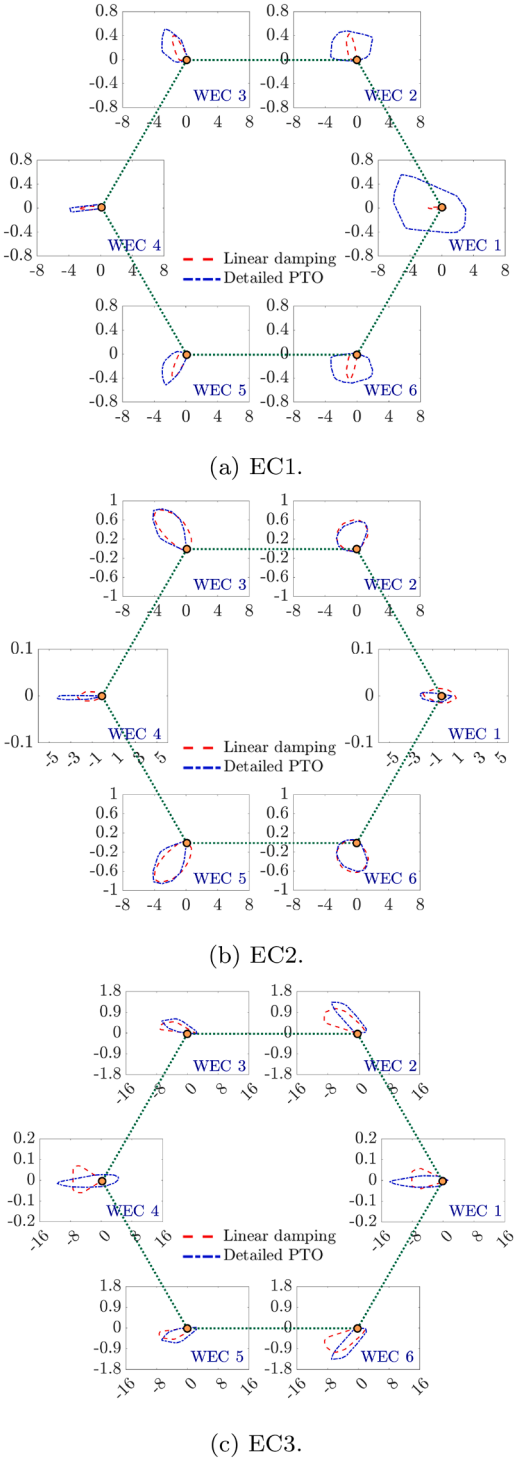

Fig. 14. WEC motion within a wave park under different ECs.

Under EC3, the power prediction from the detailed PTO system model drops significantly compared with both its power performance under EC2 and the predicted power from the linear-damper PTO system model. This is due to the restrictions imposed by the bumpers on the stroke of the water piston. It is observed in Fig. 13 that the water piston hits the bumpers frequently under EC3, causing reactive forces and energy absorption by the bumper, whereas the water piston never hits the bumpers under EC1 and EC2. In the linear-damper model, this restriction is not considered. Therefore, the power performance from the detailed PTO system model is less than that from either the detailed PTO

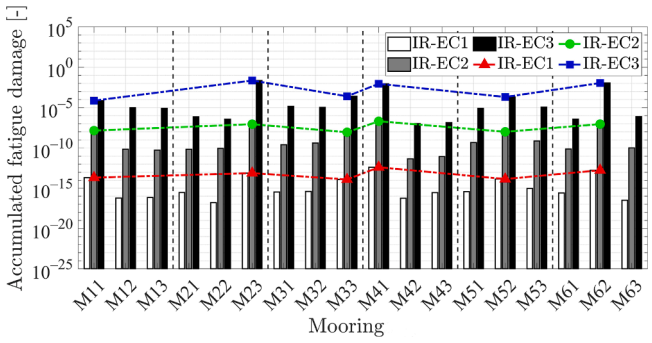

Fig. 15. Mooring fatigue damage at the fairlead under irregular waves using the detailed PTO system model. The curves show the greatest mooring fatigue damage for each WEC unit in the wave park.

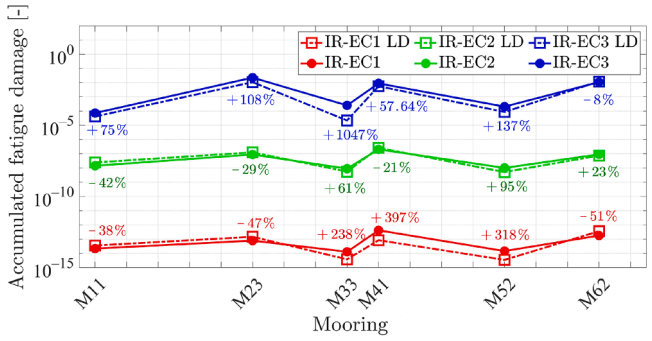

Fig. 16. Comparison of the greatest mooring fatigue damage for each WEC unit within the wave park at the fairlead under irregular waves using a linear-damper PTO model and a detailed PTO model. The difference between the two models is indicated by the percentages.

system model under EC2 or the linear-damper PTO system model under EC3.

Under IR-EC1 and IR-EC2, the power predictions from the two PTO system models are similar, which indicates a good match between the damping coefficient and the detailed PTO system model. The power prediction from the detailed PTO system model shows an overall increasing trend from IR-EC1 to IR-EC3. This means that the restriction effect from the bumper on the water piston under IR-EC3 is not as severe as that under EC3. Nevertheless, the linear-damper model under IR-EC3 yields a larger power prediction, as it does for EC3.

Overall, under wave conditions that will not activate the bumpers, the linear-damper PTO system can be calibrated by changing its damping coefficient so that it yields power predictions similar to those of the detailed PTO system model. However, the detailed PTO system model is indispensable when the bumpers are activated and provide reactive forces to the water piston, as, in this case, the power performance will greatly deteriorate due to the stroke restriction and energy absorption by the bumpers.

5.5.2. WEC Park

Fig. 18 shows the interaction factors of the wave park under the simulated wave conditions. The interaction factor is defined as the ratio of the power performance of each WEC within a wave park to the power performance of a single WEC under the same wave conditions and using the same PTO system model. Comparing the regular and irregular wave cases, an overall observation is that the irregular waves tend to even out the power performance of each WEC within the wave park due to the randomness of the wave components.

Under regular wave conditions EC1 and EC2, the linear-damper and detailed PTO system models give similar interaction factor patterns. However, under EC3, a significant difference is observed. Although the interaction factors predicted by the two models are both equally distributed among the WECs, the detailed PTO system model produces a larger interaction factor of around 1.5 than the value of around 1 obtained for the linear damper. The reason is that under EC3, as discussed in Section 5.5.1, the water piston hits the bumper, resulting in reduced power performance, whereas in the wave park under the same wave condition, the radiation and diffraction lead to a combined effect in which the water piston hits the bumper less frequently. Therefore, within the wave park, the power performance of each WEC increases compared with a single isolated WEC under EC3.

Under irregular wave condition IR-EC1, the interaction factors from the two models differ significantly. The interaction factors from the linear-damper PTO system model are less than one, indicating destructive interaction effects, whereas the detailed PTO system model predicts positive interaction effects. Although the results need to be validated through physical experiments, this major difference indicates that the fidelity level of the PTO system model has a significant influence on the interaction factor predictions for some ECs. Under IR-EC2 and IR-EC3, the two PTO system models give similar interaction factor predictions, close to one, for each WEC. This means that the power performance of the WECs is even within the wave park and that the interaction effect is negligible.

Overall, the comparison of the interaction factors from the two models shows that the fidelity level of the PTO system model influences the power performance predictions within the wave park. Validation and

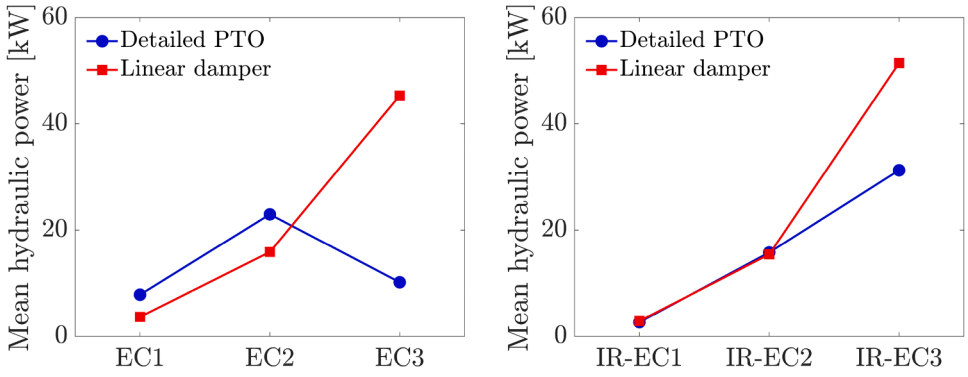

(a) Regular waves. (b) Irregular waves.

Fig. 17. Single WEC power performance under regular and irregular waves.

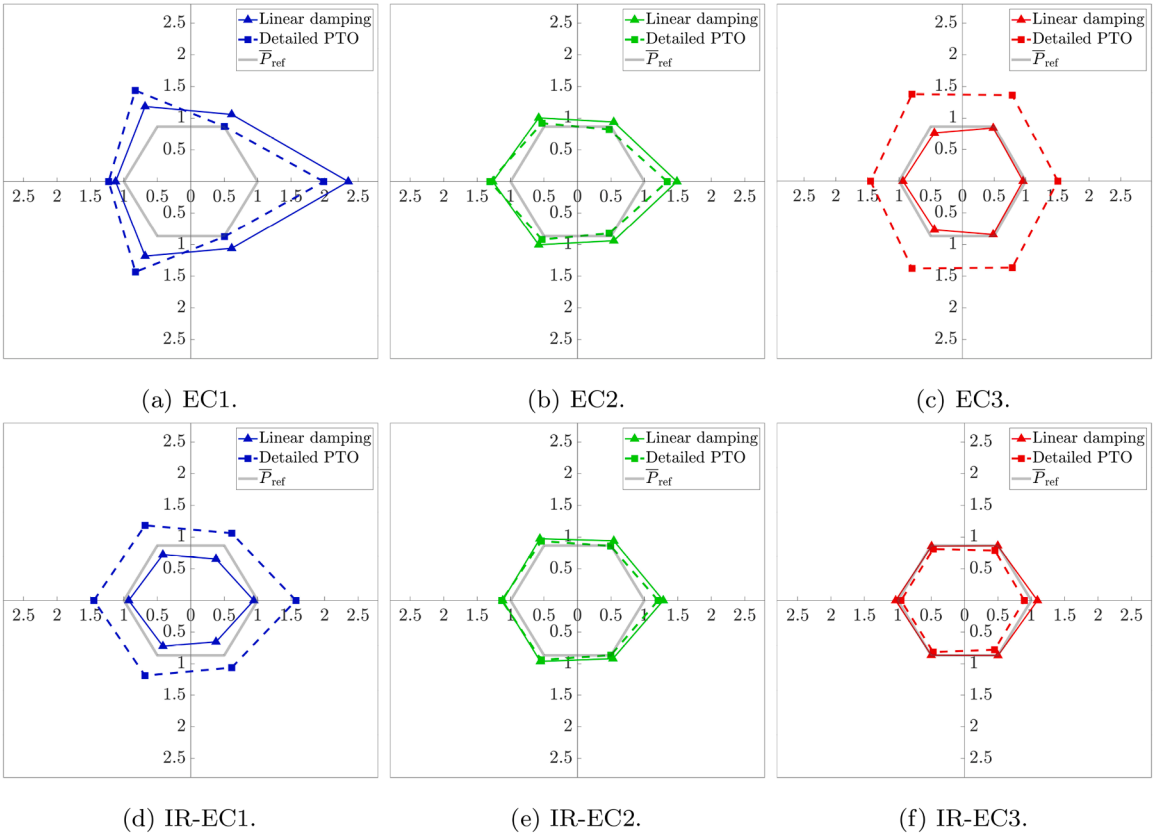

Fig. 18. Interaction factors under simulated wave conditions. The distance from each dot to the origin represents the interaction factor. The grey hexagon indicates the unit interaction factor.

calibration of the PTO system model need to be carried out through physical experiments, which will be done in future work.

6. Conclusions

This paper integrated a detailed PTO system model into WEC system simulations within an FMI-based co-simulation framework. For the first time, a co-simulation model of a six-WEC wave park was developed that incorporates a detailed PTO system model in each WEC. This model was used to investigate the influence of PTO system model fidelity on predictions of power performance and mooring force in a wave park.

The FMI-based co-simulation framework enabled the coupling of the detailed PTO system model with other subsystem models for both single-WEC and wave park simulations. The ability of FMI-based co-simulations to perform fully coupled global simulations and capture interaction effects within wave parks has been verified.

The numerical results of single WECs and wave parks have been thoroughly analysed. From the simulation results under six selected regular and irregular wave conditions, several conclusions can be made:

- Incorporating a more detailed PTO system model with higher fidelity leads to changes in the size of the WECs' watch circles, and the extent of this effect depends on the wave period and height.
- Under the simulated regular wave condition EC3 with the highest wave height, the reaction forces from the bumper can be three times larger than the PTO forces, indicating the necessity of modelling the detailed PTO system.
- The fidelity level of the PTO system model also affects the mooring fatigue damage estimation. The largest discrepancy was observed for IR-EC3, in which case the mooring fatigue damage in M33 was ten times higher when the detailed PTO system model was used.
- The comparison of interaction factors from different PTO models shows that model fidelity affects power performance predictions in a wave park.

It is recommended that future studies focusing on WEC performance and mooring force predictions should consider the PTO system model's fidelity level, which may have a large influence on the accuracy of the final results. The proposed FMI-based co-simulation framework can be applied to the modelling of other industrial applications in the renewable energy field with coupled subsystems such as wind turbines. Future work will involve validating and calibrating the PTO system model through physical experiments.

CRediT authorship contribution statement

Xinyuan Shao: Writing – review & editing, Writing – original draft, Visualization, Validation, Software, Methodology, Investigation, Formal analysis, Data curation; **Jan Forsberg:** Writing – review & editing, Methodology, Conceptualization; **Jonas W. Ringsberg:** Writing – review & editing, Supervision, Project administration, Funding acquisition.

Data availability statement

Data will be made available on request.

Declaration of competing interest

The authors declare the following financial interests/personal relationships which may be considered as potential competing interests: Jan Forsberg reports a relationship with Waves4Power AB that includes: equity or stocks. If there are other authors, they declare that they have

no known competing financial interests or personal relationships that could have appeared to influence the work reported in this paper.

Acknowledgements

This work was performed within the projects 'Control of wave energy converters based on wave measurements, for optimal energy absorption', funded by the Swedish Energy Agency through contract agreement no. 50197-1, and 'INTERACT Analysis of array systems of wave energy converters with regard to interaction effects in the LCoE and fatigue analyses', funded by the Swedish Energy Agency through contract agreement no. 50148-1. This work also received funding from the Chalmers University of Technology Foundation for the strategic research project 'Hydro- and aerodynamics'.

References

Andersson, H., Holmberg, L.J., Simonsson, K., Hilding, D., Schill, M., Borrvall, T., Sigfridsson, E., Leidermark, D., 2021. Simulation of leakage flow through dynamic sealing gaps in hydraulic percussion units using a co-simulation approach. Simul. Model. Pract. Theory 111, 102351. https://doi.org/10.1016/j.simpat.2021.102351.

Ansys, 2023a. Ansys Aqwa (Version 2023 R1) [software]. (accessed 24 February 2025), https://www.ansys.com/products/.

Ansys, 2023b. Ansys rigid dynamics (Version 2023 R1) [software]. (accessed 24 February 2025), https://www.ansys.com/products/structures/ansys-motion.

Bao, J., Yu, D., 2024. Hydrodynamic performance optimization of a cost-effective WEC-type floating breakwater with half-airfoil bottom. Renew. Energy 226, 120333. https://doi.org/10.1016/j.renene.2024.120333.

Cao, F.F., Yu, M.Q., Han, M., Liu, B., Wei, Z.W., Jiang, J., Tian, H.Y., Shi, H.D., Li, Y.N., 2023. WECs Microarray effect on the coupled dynamic response and power performance of a floating combined wind and wave energy system. Renew. Energy 219, 119476. https://doi.org/10.1016/j.renene.2023.119476.

Chen, Z., Sun, J., Yang, J., Sun, Y., Chen, Q., Zhao, H., Qian, P., Si, Y., Zhang, D., 2024. Experimental and numerical analysis of power take-off control effects on the dynamic performance of a floating wind-wave combined system. Renew. Energy 226, 120353. https://doi.org/10.1016/j.renene.2024.120353.

Cummins, W.E., 1962. The Impulse Response Function and Ship Motions. Technical Report 1661. Department of the Navy, David Taylor Model Basin, Bethesda, MD, USA

DNV, 2021. Offshore Standards Position Mooring. Technical Report. Det Norske Veritas (DNV).

Falcao, A.F., 2010. Wave energy utilization: a review of the technologies. Renew. Sustain. Energy Rev. 14 (3), 899–918.

Gan, J., Zhou, Z., Yu, A., Ellis, D., Attwood, R., Chen, W., 2023. Co-simulation of multibody dynamics and discrete element method for hydraulic excavators. Powder Technol. 414, 118001. https://doi.org/10.1016/j.powtec.2022.118001.

Gomes, C., Thule, C., Broman, D., Larsen, P.G., Vangheluwe, H., 2018. Co-simulation: a survey. ACM Comput. Surv. 51 (3), 1–33. https://doi.org/10.1145/3179993.

Han, M., Shi, H., Cao, F., Zhu, K., Liu, B., Yu, M., Wei, Z., 2024. Dynamic characteristics and parameter analysis of a floating hybrid wind-wave energy system based on a novel coupled numerical framework. Energy Convers. Manage. 312, 118558. https://doi.org/10.1016/j.enconman.2024.118558.

Hatledal, L.I., Skulstad, R., Li, G., Styve, A., Zhang, H., 2020. Co-simulation as a fundamental technology for twin ships. Model. Identif. Control: Nor. Res. Bull. 41 (4), 297–311. https://doi.org/10.4173/mic.2020.4.2.

International Energy Agency, 2023. World energy outlook 2023.

Jin, P., Zheng, Z., Zhou, Z., Zhou, B., Wang, L., Yang, Y., Liu, Y., 2023. Optimization and evaluation of a semi-submersible wind turbine and oscillating body wave energy converters hybrid system. Energy 282, 128889. https://doi.org/10.1016/j.energy.2023.128889.

Lee, S.C., Song, S., Park, S., 2021. Platform motions and mooring system coupled solver for a moored floating platform in a wave. Processes 9 (8), 1393. https://doi.org/10.3390/pr9081393.

Li, X., Xiao, Q., Zhou, Y., Ning, D., Incecik, A., Nicoll, R., McDonald, A., Campbell, D., 2022. Coupled CFD-MBD numerical modeling of a mechanically coupled WEC array. Ocean Eng. 256, 111541. https://doi.org/10.1016/j.oceaneng.2022.111541.

Mathworks, 2024. Simulink is for model-based design (version R2024A). (accessed 24 February 2025), https://se.mathworks.com/products/simulink.HTML.

Modelica Association, 2024. FMI Tools. (accessed 24 February 2025), https://fmi-standard.org/tools/.

Ogilvie, T.F., 1964. Recent progress toward the understanding and prediction of ship motions. In: Proceedings of the Fifth Symposium on Naval Hydrodynamics, Bergen, Norway, pp. 3–79.

Quartier, N., Vervaet, T., Fernandez, G.V., Domínguez, J.M., Crespo, A. J.C., Stratigaki, V., Troch, P., 2024. High-fidelity numerical modelling of a two-WEC array with accurate implementation of the PTO system and control strategy using dualSPHysics. Energy 296, 130888. https://doi.org/10.1016/j.energy.2024.130888.

Rychlik, I., 1987. A new definition of the rainflow cycle counting method. Int. J. Fatigue 9 (2), 119–121. https://doi.org/10.1016/0142-1123(87)90054-5.

Saccomandi, G., Ogden, R.W., 2004. Mechanics and Thermomechanics of Rubberlike Solids. Springer.

Shao, X., Ringsberg, J.W., Johnson, E., Li, Z., Yao, H.-D., Skjoldhammer, J.G., Björklund, S., 2025. An FMI-based co-simulation framework for simulations of wave energy converter systems. Energy Convers. Manage. 323, 119220.

Shao, X., Ringsberg, J.W., Yao, H.-D., Gowda, U. R. S.L., Khedkar, H.N., Todalshaug, J.H., 2024a. Hydrodynamic interactions and enhanced energy harnessing amongst many WEC units in large-size wave parks. J. Mar. Sci. Eng. 12 (5), 730. https://doi.org/10.3390/jmse12050730.

Shao, X., Ringsberg, J.W., Yao, H.-D., Li, Z., Johnson, E., Fredriksson, G., 2023. A comparison of two wave energy converters' power performance and mooring fatigue characteristics – one WEC vs many WECs in a wave park with interaction effects. J. Ocean Eng. Sci. 8 (4), 446–460. https://doi.org/10.1016/j.joes.2023.07.007.

Shao, X., Yao, H.-D., Ringsberg, J.W., Li, Z., Johnson, E., 2024b. Performance analysis of two generations of heaving point absorber WECs in farms of hexagon-shaped array layouts. Ships Offshore Struct. 19, 1–12. https://doi.org/10.1080/17445302.2024.2317658.

Venzke, M., Shudrenko, Y., Youssfi, A., Steffen, T., Turau, V., Becker, C., 2023. Co-simulation of a cellular energy system. Energies 16 (17), 6150. https://doi.org/10.3390/en16176150.

Wang, T., Zhu, K., Cao, F., Li, D., Gong, H., Li, Y., Shi, H., 2024. A coupling framework between openFAST and WEC-Sim. Part I: validation and dynamic response analysis of IEA-15-MW-UMaine FOWT. Renew. Energy 225, 120249. https://doi.org/10.1016/j.renene.2024.120249.

Waves4Power, 2024. Homepage. (accessed 24 February 2025), https://www.waves4power.com/.

Yang, Y., Bashir, M., Michailides, C., Li, C., Wang, J., 2020. Development and application of an aero-hydro-servo-elastic coupling framework for analysis of floating offshore wind turbines. Renew. Energy 161, 606–625. https://doi.org/10.1016/j.renene.2020.07.134.

Yuan, R., Fletcher, T., Ahmedov, A., Kalantzis, N., Pezouvanis, A., Dutta, N., Watson, A., Ebrahimi, K., 2020. Modelling and co-simulation of hybrid vehicles: a thermal management perspective. Appl. Therm. Eng. 180, 115883. https://doi.org/10.1016/j.applthermaleng.2020.115883.

Zeinali, S., Wiktorsson, M., Forsberg, J., Lindgren, G., Lindström, J., 2024. Optimizing the hydraulic power take-off system in a wave energy converter. Ocean Eng. 310, 118636. https://doi.org/10.1016/j.oceaneng.2024.118636.

Zhang, D., Chen, Z., Liu, X., Sun, J., Yu, H., Zeng, W., Ying, Y., Sun, Y., Cui, L., Yang, S., Qian, P., Si, Y., 2022. A coupled numerical framework for hybrid floating offshore wind turbine and oscillating water column wave energy converters. Energy Convers. Manage. 267, 115933. https://doi.org/10.1016/j.enconman.2022.115933.